NANO LETTERS

pubs.acs.org/NanoLett Letter

Imaging Strain-Controlled Magnetic Reversal in Thin CrSBr

Kousik Bagani,[▽] Andriani Vervelaki,[▽] Daniel Jetter, Aravind Devarakonda, Märta A. Tschudin, Boris Gross, Daniel G. Chica, David A. Broadway, Cory R. Dean, Xavier Roy, Patrick Maletinsky, and Martino Poggio*

Cite This: https://doi.org/10.1021/acs.nanolett.4c03919 Read Online

ACCESS | Metrics & More | Article Recommendations | Supporting Information

ABSTRACT: Two-dimensional materials are extraordinarily sensitive to external stimuli, making them ideal for studying fundamental properties and for engineering devices with new functionalities. One such stimulus, strain, affects the magnetic properties of the layered magnetic semiconductor CrSBr to such a degree that it can induce a reversible antiferromagnetic-to-ferromagnetic phase transition. Using scanning SQUID-on-lever microscopy, we directly image the effects of spatially inhomogeneous strain on the magnetization of layered CrSBr, as it is polarized by a field applied along its easy axis. The evolution of this magnetization and the formation of domains is reproduced by a micromagnetic model, which incorporates the spatially varying strain and the corresponding changes in the local interlayer exchange stiffness. The observed sensitivity to small strain gradients along with similar images of a nominally unstrained CrSBr sample suggest that unintentional strain inhomogeneity influences the magnetic behavior of exfoliated samples.

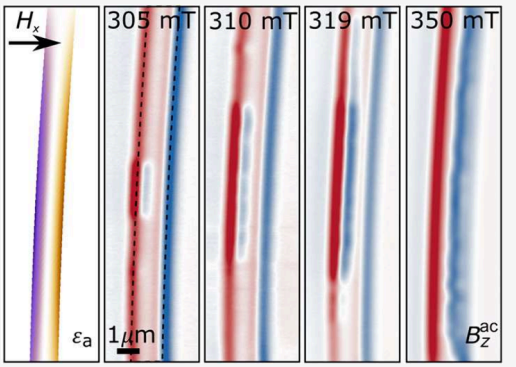

KEYWORDS: *2D magnetism, CrSBr, scanning SQUID microscopy, magnetic field imaging, strain engineering*

The study of two-dimensional (2D) materials and their heterostructures has revealed a diverse array of electronic, optical, and magnetic properties, paving the way for groundbreaking advancements in condensed matter physics and materials science. These ultrathin materials are exceptionally sensitive to external stimuli, such as strain, doping, and electromagnetic fields, each of which can be used to influence or control their properties. This responsiveness extends to 2D magnets, affecting parameters such as the ordering temperature, magnetic coercivity, magnetic anisotropy—potentially even altering the magnetic easy axis or triggering magnetic phase transitions.[1−5]

CrSBr is a layered van der Waals material and an A-type antiferromagnet with a Néel temperature of $T_N \approx 132$ K in the bulk.[6,7] Its magnetic anisotropy is triaxial with both its intermediate and easy axes pointing in the layer plane, along the crystallographic *a*- and *b*-axis, respectively.[6] It stands out as a direct bandgap semiconductor with strong magneto-electronic coupling[7,8] and tunable magnetic properties.[9−12] In addition, unlike the extensively studied Cr-trihalide family of 2D magnets,[13−15] it displays excellent air stability,[7,16,17] simplifying device fabrication and experimental investigation.

The response of CrSBr to mechanical strain is particularly noteworthy: the application of strain along its *a*-axis modifies its magnetic properties, with the most significant change occurring in the interlayer exchange interaction. Specifically, compressive strain has been predicted to enhance the antiferromagnetic (AF) interlayer interaction, whereas tensile strain reduces this coupling, eventually converting it from AF to ferromagnetic (F).[9,18−21] In fact, a controllable and reversible strain-induced AF-to-F phase transition has been reported under an applied uniaxial strain exceeding 1%. This observation demonstrates the potential of CrSBr as the active element in devices, such as magnetoresistive switches or magnetic tunnel junctions, that are actuated by strain rather than applied magnetic field.[9,10] So far, however, locally resolved measurements of how spatially varying strain or strain intrinsic to exfoliated samples influences the magnetic properties of CrSBr have not been carried out.

Here, we directly image the impact of strain on magnetic reversal in CrSBr flakes. Using a cantilever scanning probe with an integrated superconducting quantum interference device (SQUID), we map how nonuniform strain alters the magnetic hysteresis and influences the formation and evolution of magnetic domains. To distinguish the effects of strain from the intrinsic behavior of thin CrSBr, we compare the behavior of strained and pristine flakes with similar geometries. Furthermore, we use a micromagnetic model to simulate the magnetic

Received: August 14, 2024
Revised: September 27, 2024
Accepted: September 30, 2024

https://doi.org/10.1021/acs.nanolett.4c03919
Nano Lett. XXXX, XXX, XXX−XXX

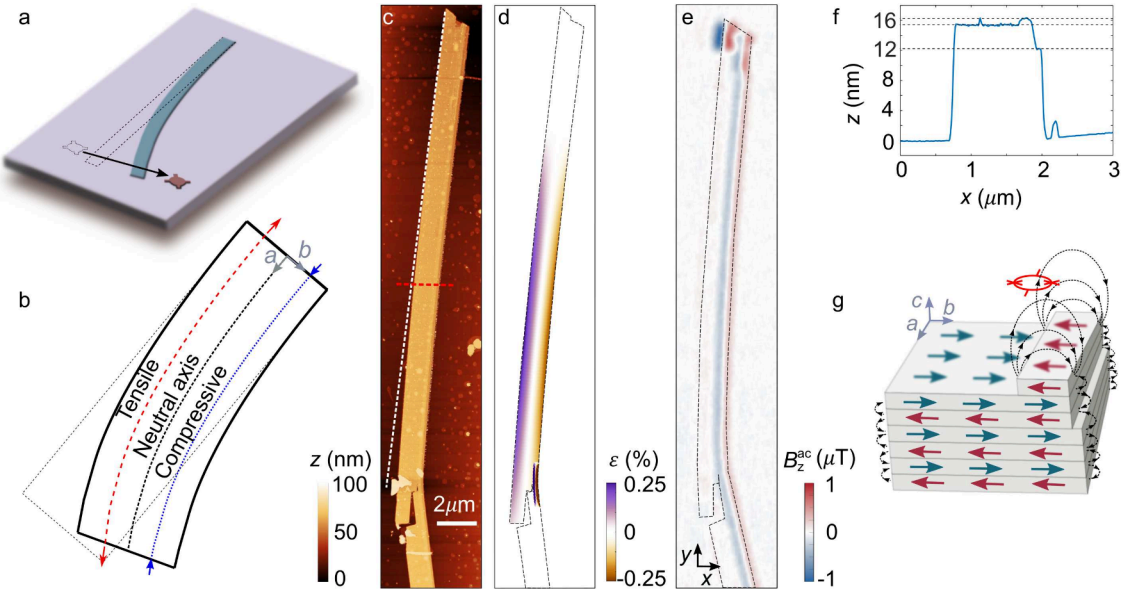

Figure 1. Strained CrSBr ribbon. Schematic of (a) the bending procedure using a micromanipulator and (b) the resulting strain. (c) An atomic force microscopy (AFM) image of the CrSBr ribbon after bending and (d) a map of the calculated strain induced by this bending procedure. The white dashed line in panel (c) represents the initial shape of the ribbon before the bending. (e) $B_z^{ac}(x,y)$ measured in the absence of in-plane applied field. The *x*- and *y*-axis correspond to the coordinates of the scanning probe. (f) A line-cut across the AFM image taken along the dashed red line in panel (c). The black dashed lines indicate the different thicknesses—14, 18, and 19 layers—found within the ribbon. (g) Schematic drawing of the ribbon's AF magnetization configuration (showing fewer layers than in the actual ribbon) with magnetization shown in red and blue arrows and stray field lines as black dotted arrows. The red symbol represents the SQUID-on-lever scanning probe. The crystallographic *a*-, *b*-, and *c*-axes of CrSBr are represented by gray arrows.

evolution of a strained flake, reproducing both the spatial and field-dependent features of our measurements and gaining insight into the underlying magnetization configurations. The results show how local variations of strain can be used to create magnetic domains on demand. Moreover, they highlight the sensitivity of 2D magnetic systems to strain and how unintentional strain gradients, induced during sample fabrication or processing, can result in inhomogeneous behavior.

Exfoliated CrSBr flakes naturally form a ribbon shape due to their anisotropic crystal structure. The long edge aligns with the crystallographic *a*-axis, the short edge with the *b*-axis, and the *c*-axis points out of the plane. This geometry is ideal for the application of in-plane strain by physically bending the ribbon. Using a recently developed method,[22] we position a gear-shaped graphite microstructure adjacent to one end of a CrSBr ribbon. We then slide the microstructure over one end of the ribbon using the tip of an atomic force microscopy (AFM) cantilever, as shown in Figure 1a. This action drags the end of the ribbon along with the manipulator, while the opposing end remains firmly secured to the substrate. The result is a bent ribbon that is elongated on one side and compressed on the other, as shown in Figure 1b, thereby generating tensile and compressive strain, respectively, along the *a*-axis. Figure 1c shows a topographic image of such a bent CrSBr ribbon with a fracture in its lower segment due to excessive bending. We calculate a map of the resulting inhomogeneous strain, shown in Figure 1d, by measuring its topographic outline and extracting the local radius of curvature (Supporting Information 1.2).[22]

We image the out-of-plane component of the strained ribbon's magnetic stray field B_z in a plane 250 nm above the sample at 4.2 K. Measurements are carried out using a SQUID-on-lever scanning probe,[23] which, in addition to B_z, allows for the measurement of $B_z^{ac} \propto dB_z/dz$ by demodulating the SQUID response at the cantilever oscillation frequency. Due to spectral filtering, B_z^{ac} contains less noise than B_z. Figure 1e shows $B_z^{ac}(x,y)$ measured in the absence of an applied in-plane magnetic field. The image shows magnetic contrast that is primarily confined to the right edge of the ribbon.

Without an applied in-plane field, the strained ribbon should be in an AF configuration with the magnetization of each successive layer pointing along the *b*-axis and alternating its orientation. Based on previous findings,[9] the magnitude of the applied strain is not sufficient to change this AF remanent configuration. Therefore, we expect regions with an even number of layers to produce no stray field, because the magnetization of adjacent AF layers exactly compensate, whereas regions with odd number of layers should produce a stray field equivalent to that of one uncompensated layer.

We compare our measurements to this expectation by determining the ribbon's layer thickness via AFM, as shown in Figure 1c. A line-cut of this AFM, plotted in Figure 1f, shows that the majority of the ribbon consists of 18 layers, except for a single-layer strip 350 nm wide running along its right edge. To the right of this strip is a 210-nm-wide region, which is 14 layers thick. Therefore, we attribute the dipolar magnetic contrast observed near the right edge of the ribbon to the single uncompensated layer along the right edge of the ribbon and show the corresponding magnetization configuration schematically in Figure 1g. Aside from this strip, the rest of the ribbon is fully compensated and produces no magnetic contrast. An exception is the region near the top end of the ribbon, where the thickness is not uniform.

We next image the stray magnetic field produced by both strained and pristine CrSBr ribbons under increasing in-plane applied magnetic field. We apply H_x nearly along the *b*-axis of each ribbon. As revealed from AFM measurements, shown in

https://doi.org/10.1021/acs.nanolett.4c03919
Nano Lett. XXXX, XXX, XXX−XXX

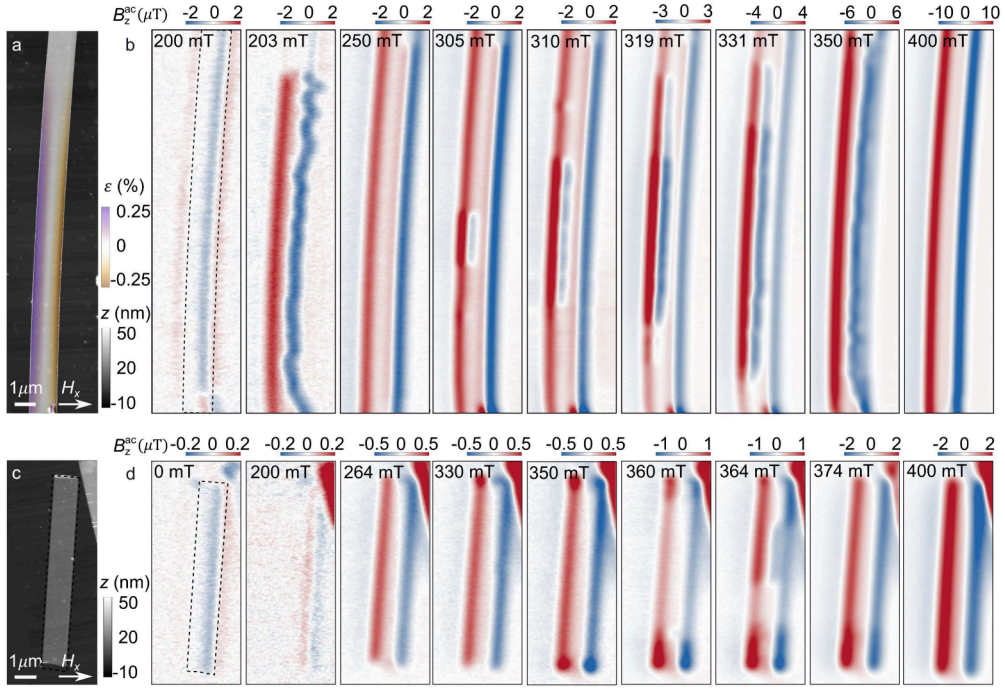

Figure 2. Magnetic field dependence of strained and pristine ribbons. (a) An expanded AFM image of the strained ribbon presented in Figure 1c overlaid with a map of the calculated strain. (b) $B_z^{ac}(x,y)$ measured over this region under increasing in-plane applied field $\mu_0 H_x$, as indicated in the top left of each image. Dashed outlines in the first field map denote the physical boundaries of the ribbon. (c) AFM image of the pristine ribbon and (d) the corresponding $B_z^{ac}(x,y)$ measured under increasing $\mu_0 H_x$.

Figures 2a and 2c, the pristine ribbon is 18 layers thick with an additional narrow single layer along the right edge, like the strained ribbon. Before imaging, we initialize the magnetic state of both ribbons by saturating the magnetization along the *b*-axis with an applied field $\mu_0 H_x = -500$ mT. We then sweep the field to zero before incrementally increasing it and imaging $B_z^{ac}(x,y)$ up to $\mu_0 H_x = 600$ mT. In low applied field $\mu_0 H_x < 100$ mT, both ribbons remain in an AF state, with their only magnetic contrast due to the uncompensated strip near each ribbon's right edge, as observed in Figures 2b and 2d. Further increases of H_x, however, result in a different evolution of the magnetic state in each ribbon.

In the strained ribbon, as shown in Figure 2b, a magnetization reorientation process occurs at $\mu_0 H_x = 203$ mT, producing a clear signature in B_z^{ac}, corresponding to uncompensated magnetization pointing along the applied field. Although most of the ribbon is covered by this contrast, a section near the top of the image and an area along the right edge of the ribbon remain in the AF configuration. The wavy vertical features delineate the boundary between uncompensated and AF regions and are discussed below. Upon increasing $\mu_0 H_x$, the uncompensated region gradually expands throughout the ribbon, covering it almost completely at $\mu_0 H_x = 225$ mT (Figure S3e). Here, the magnitude of $B_z^{ac}(x,y)$ corresponds to that expected for two uncompensated magnetic layers. From this image, we infer that the ribbon's bottom layer flips along the applied field, resulting in two full uncompensated layers (bottom and top) aligned along the field, while most of the single narrow uncompensated strip along the right edge remains oriented against the applied field. We assume the bottom layer to flip, because surface layers couple to only one adjacent layer, resulting in a lower energetic cost for reorientation than interior layers,[10,24,25] while the top layer is already oriented along the field opposing the narrow uncompensated strip. By $\mu_0 H_x = 250$ mT, both the bottom layer and the narrow single-layer strip have fully oriented along the field. Upon further increase of the field, at $\mu_0 H_x = 305$ mT, a small region of uncompensated magnetization forms where the tensile strain is largest, as shown in Figure 2b. The magnetic contrast corresponds to that of two further uncompensated layers, indicating the flipping of an interior layer. As shown in Figure 2b, subsequent increases in H_x—especially between $\mu_0 H_x = 310$ and 350 mT—result in the expansion of this contrast along the left edge of the ribbon, accompanied by discrete increases in its magnitude, which emerge from the region of largest tensile strain. The behavior is consistent with additional layers orienting along the field, starting from the region of largest tensile strain. Eventually, the polarized region propagates across the entire ribbon, saturating around $\mu_0 H_x = 400$ mT.

In the pristine ribbon, as shown in Figure 2d, no magnetization reorientation is visible up to $\mu_0 H_x = 100$ mT, at which point the narrow uncompensated strip along the right edge flips along the field (Figure S5b). At $\mu_0 H_x = 264$ mT, an abrupt transition occurs throughout the sample. As in the strained case, the contrast corresponds to two uncompensated layers, indicating the flipping of the bottom layer. As shown in Figure 2d, this configuration persists until $\mu_0 H_x = 330$ mT, at which point contrast corresponding to the reorientation of an additional flipped layer appears near the top end of the ribbon. At $\mu_0 H_x = 350$ mT, similar contrast appears near the bottom end, followed by its expansion from both ends toward the middle of the ribbon. In this process, the magnitude of the contrast increases, indicating the reorientation of additional layers. The ribbon eventually saturates around $\mu_0 H_x = 400$ mT. Note that the strong magnetic contrast visible in the top right corner of the images in Figure 2d originates from a nearby thick flake.

https://doi.org/10.1021/acs.nanolett.4c03919
Nano Lett. XXXX, XXX, XXX−XXX

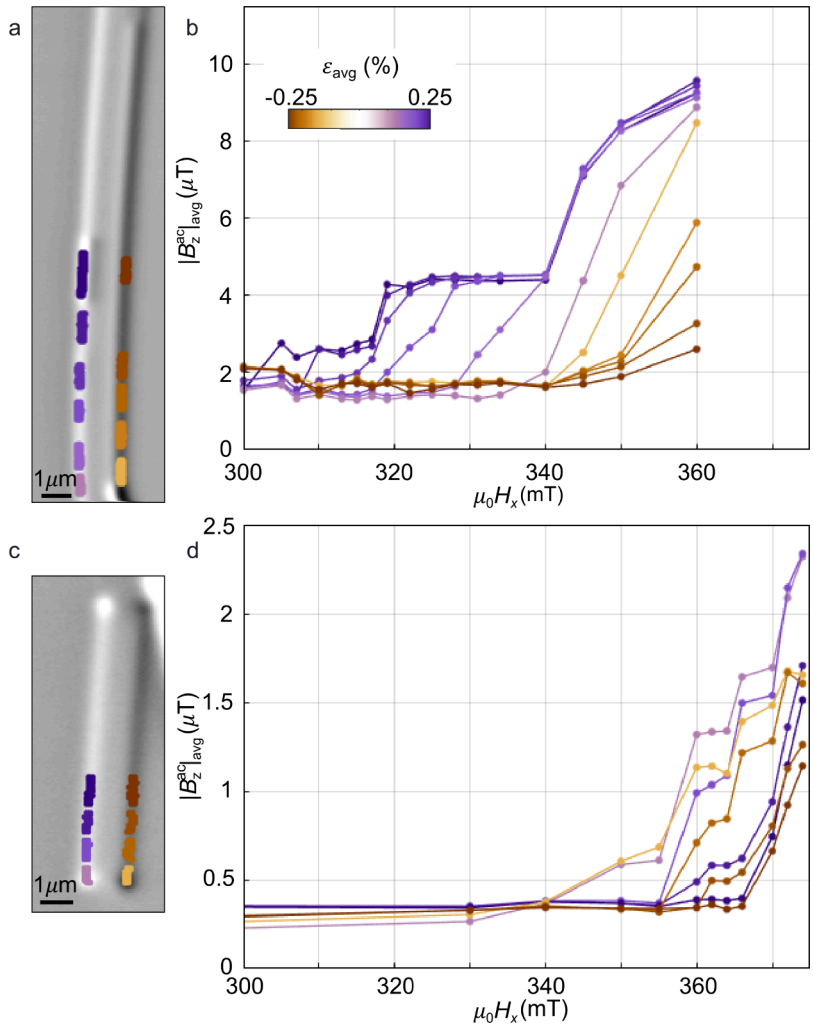

Figure 3. Strain-dependent reversal. (a) $B_z^{ac}(x,y)$ map of the strained ribbon with $\mu_0 H_x$ = 305 mT. (b) $|B_z^{ac}|_{avg}$ plotted as a function of increasing $\mu_0 H_x$ averaged over the color-coded areas in panel (a), corresponding to different average *a*-axis strain (shown as a percentage in the legend). (c) $B_z^{ac}(x,y)$ map of the pristine ribbon with $\mu_0 H_x$ = 350 mT and (d) $|B_z^{ac}|_{avg}$, plotted as a function of increasing $\mu_0 H_x$ averaged over the color-coded areas presented in panel (c).

The inhomogeneously strained ribbon, initially in its AF state, is polarized layer-by-layer by a magnetic field applied along its easy axis. As shown in Figure 2b, this reorientation begins in regions of the largest tensile strain, which weakens the interlayer AF coupling, eventually expanding into regions of compressive strain, which enhances the AF interaction. Tuning the interlayer coupling more strongly influences the magnetic reversal of interior layers than surface layers, due to their coupling with an additional adjacent layer. This is evidenced by the more abrupt polarization of the surface layer in Figure 2b. In the pristine ribbon, the same reversal process, shown in Figure 2d, begins at a higher field, i.e., $\mu_0 H_x$ = 264 instead of 203 mT, because of the lack of tensile strain weakening the AF interaction. The reversal also occurs over a narrower field range, due to less strain inhomogeneity compared to the strained ribbon. Only the narrow single-layer found along the right edge of both ribbons is observed to flip in the pristine ribbon first: at $\mu_0 H_x$ = 100 mT in the pristine ribbon compared to 225 mT in the strained ribbon. In the strained ribbon, this strip experiences compressive strain, enhancing the interlayer AF interaction and thus increasing its switching field relative to the strip on the pristine ribbon.

Plotting the local magnetic response of different regions of the sample makes the effect of strain on magnetic reversal apparent. Figure 3a highlights regions in the strained ribbon with different average strain along the *a*-axis and Figure 3b shows their average $|B_z^{ac}|$, as a function of $\mu_0 H_x$. A strong correlation is evident between the magnetic switching behavior of different regions of the ribbon—as indicated by each local $|B_z^{ac}|_{avg}(H_x)$ curve—and their corresponding strain. Specifically, the field required to initiate the reorientation process increases with increasing compressive strain: the regions with the most tensile strain switch first, while those with the most compressive switch last. The reorientation of the first two interior layers is clearly visible in Figure 3b as two discrete steps in the stray field from the regions corresponding to the most tensile strain. Subsequent steps or similar behavior in less-strained regions occur in a narrower range of H_x and are therefore not resolved over the measured applied field interval.

Figures 3c and 3d highlight different regions of the unstrained ribbon and show their local magnetic response. The $|B_z^{ac}|_{avg}(H_x)$ curves show significantly less variation in switching fields than in the strained ribbon. Although steps in

https://doi.org/10.1021/acs.nanolett.4c03919
Nano Lett. XXXX, XXX, XXX−XXX

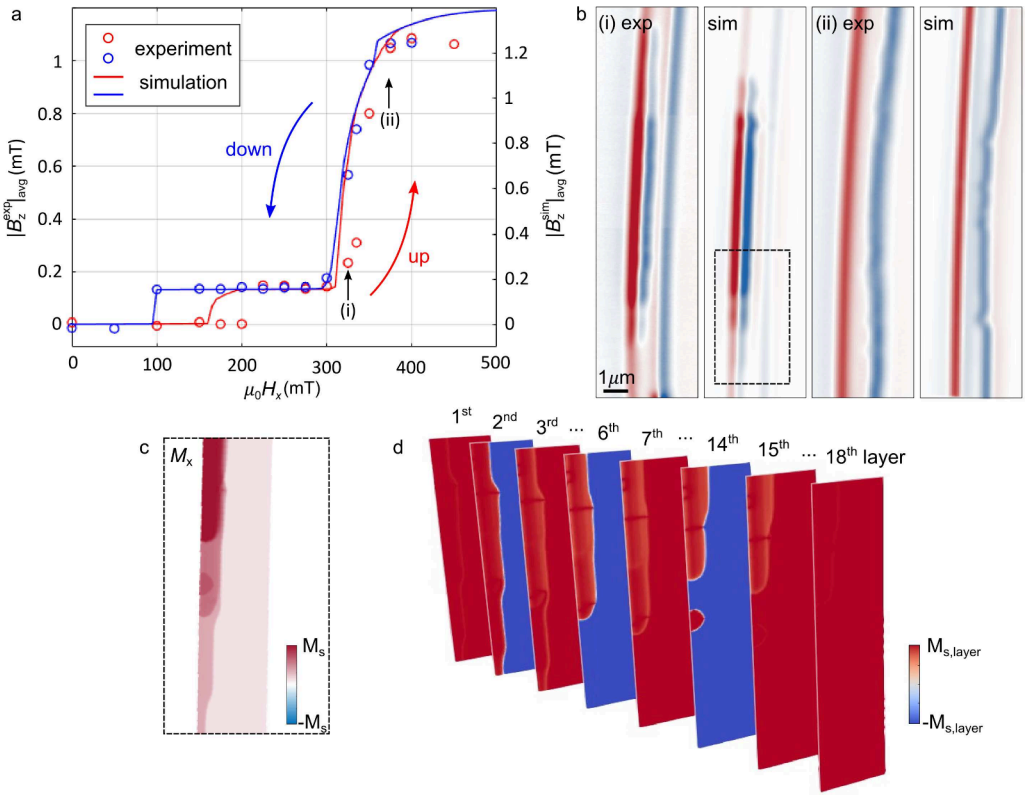

Figure 4. Visualizing the magnetization configuration during reversal. (a) A comparison between experimental and simulated magnetic hysteresis for the strained ribbon. The vertical axis corresponds to $|B_z|$ averaged over the entire imaging area shown in each subpanel of panel (b), which includes the central part of the ribbon. (b) The domains observed in the experimental $B_z^{ac}(x,y)$ maps are compared to the ones produced by the simulated $\frac{dB_z(x,y)}{dz}$ under (i) $\mu_0 H_x$ = 322 mT in the experiment and $\mu_0 H_x$ = 315 mT in the simulation and (ii) $\mu_0 H_x$ = 375 mT for both experiment and simulation. (c) The total magnetization along the x-axis, $M_x(x, y)$, for the region indicated by the black dotted box in panel (b). M_s represents the total saturation magnetization across all 18 layers. The magnetization of this area is also plotted for selected layers in panel (d). $M_{s,\,layer}$ denotes the saturation magnetization of a single layer.

$|B_z^{ac}|_{avg}(H_x)$, which correspond to the reorientation of individual layers, are recognizable in some regions, most occur over such small ranges in H_x that the measurement does not resolve them. Despite the absence of intentional strain, the $|B_z^{ac}|_{avg}(H_x)$ curves show a noticeable trend of increasing switching field from the bottom and top edges toward the center of the pristine ribbon. Given the sensitivity of magnetic reversal to small strain gradients in the strained ribbon (down to fractions of a percent per micrometer), this spatial dependence could be the result of unintentional strain inhomogeneity. Although the switching behavior near the top end of the ribbon could be influenced by the stray field of a neighboring flake, seen in the top right of Figure 3c, similar behavior observed near the bottom end of the ribbon makes this possibility unlikely. Crystal growth, exfoliation, or the process of transferring the ribbon to the substrate may induce inhomogeneous strain in the sample.[10,26,27]

To visualize the magnetic configurations underlying our measured stray-field maps, we perform micromagnetic simulations based on the Landau–Liftshitz–Gilbert formalism.[28,29] We simulate the main part of the 18-layer-thick bent ribbon using its geometry, as determined from AFM images and known material parameters. We implement a locally varying interlayer exchange stiffness $A_{ex,inter}$, based on the map of applied a-axis strain, shown in Figure 1d, and the theoretical dependence of $A_{ex,inter}$ on strain.[18] Figures 4a and 4b show how simulations of the strained ribbon reproduce both the observed magnetic hysteresis and the measured $B_z^{ac}(x,y)$ maps as the strained ribbon is polarized by a field applied along its easy axis. Simulations were also carried out assuming both position-dependent magnetocrystalline anisotropy of the a-axis (K_a) and strain-dependent intralayer exchange stiffness ($A_{ex,intra}$), but neither reproduced the measurements.

The simulations confirm that the first layer to flip along the applied field, seen in both measured and simulated hysteresis curves as a step around $\mu_0 H$ = 200 mT in Figure 4a, is indeed a surface layer (bottom or top, depending on the initial AF configuration). They also explain specific features in maps of $B_z^{ac}(x,y)$ observed during reversal. In particular, they reproduce both the initiation of magnetic reorientation in the region of largest tensile strain and its expansion out from this area. As seen in Figure 4b, even the wavy features observed in $B_z^{ac}(x,y)$ maps at the borders of polarized domains appear in simulated images of similar configurations. These features correspond to boundaries extending through the thickness of the ribbon between regions with different numbers of uncompensated layers, as seen in Figures 4c and 4d. These boundaries arise because of the spatially varying strain and its effect on $A_{ex,inter}$. Since the simulations only consider this spatial dependence in the sample, we conclude that these boundaries are not due to other inhomogeneities, imperfections, or defects in the ribbon itself. The simulations also reproduce layer-by-layer switching without accounting for any vertical strain gradients as

https://doi.org/10.1021/acs.nanolett.4c03919
Nano Lett. XXXX, XXX, XXX−XXX

suggested in ref 10. To minimize the demagnetization field during polarization and because interlayer coupling is much weaker than intralayer, the ribbon flips one layer at a time rather than all at once. Moreover, according to the simulations, the domain walls between the oppositely polarized domains are Néel-type, as was observed by Zur et al.[30]

Similar simulations of the pristine ribbon using its measured geometry, thickness, and uniform parameters—including $A_{ex,inter}$—do not reproduce the observed reorientation behavior. In particular, simulations do not show reversal proceeding through spatially confined domains of uncompensated magnetization. Rather, the entire ribbon goes through a reorientation over a much narrower range of H_x than in the measurements. Reorientation that begins at the top and bottom ends of the ribbon can therefore not be explained by the geometry of the sample and the resulting inhomogeneity in its demagnetization field. However, the simulations do display behavior similar to the measurements upon the introduction of a spatially varying $A_{ex,inter}$ near the top and bottom of the ribbon, supporting the hypothesis of unintentional strain at the ends.

We show both the unambiguous coupling of strain to magnetic reversal and the ability to locally tune the interlayer exchange stiffness via strain. Such local control over the magnetic properties of a 2D magnet could be used in devices to program the formation of domains or to spatially confine magnetic reversal. The evolution of magnetization, as a function of applied field and position, are well-described by a linear magnetoelastic coupling between *a*-axis strain and interlayer exchange. Although strain gradients are responsible for the formation of domains of compensated and uncompensated magnetization, we do not find evidence for purely flexomagnetic effects, i.e., effects coupling strain gradients and magnetization directly.[31] However, given the large strain gradients that can be achieved in such bent ribbons, they form the ideal platform for revealing the presence and strength of flexomagnetic effects in other vdW systems. Measurements also suggest that small strain gradients—in some cases, unintentional—can affect the sample's magnetic hysteresis. These gradients could be produced by the exfoliation and deposition process, and they can result in an inhomogeneous evolution of magnetic hysteresis throughout the sample. Sensitivity to unintentional strain must therefore be considered in the design of magnetic devices involving CrSBr or similar materials. The effects of unintentional strain may explain inhomogeneities observed in previous spatially resolved[12,17,32] and transport[33] measurements.

■ ASSOCIATED CONTENT

Supporting Information

The Supporting Information is available free of charge at https://pubs.acs.org/doi/10.1021/acs.nanolett.4c03919.

Methods: CrSBr ribbons, map of inhomogeneous strain, SQUID-on-lever, magnetic imaging, micromagnetic simulations; Additional measurements and simulations: topographic imaging, magnetic imaging, magnetic hysteresis, micromagnetic simulations (PDF)

■ AUTHOR INFORMATION

Corresponding Author

Martino Poggio − *Department of Physics and Swiss Nanoscience Institute, University of Basel, 4056 Basel, Switzerland;* orcid.org/0000-0002-5327-051X; Email: martino.poggio@unibas.ch

Authors

Kousik Bagani − *Department of Physics, University of Basel, 4056 Basel, Switzerland*

Andriani Vervelaki − *Department of Physics, University of Basel, 4056 Basel, Switzerland*

Daniel Jetter − *Department of Physics, University of Basel, 4056 Basel, Switzerland*

Aravind Devarakonda − *Department of Physics, Columbia University, New York, New York 10027, United States; Department of Applied Physics and Applied Mathematics, Columbia University, New York, New York 10027, United States*

Märta A. Tschudin − *Department of Physics, University of Basel, 4056 Basel, Switzerland*

Boris Gross − *Department of Physics, University of Basel, 4056 Basel, Switzerland*

Daniel G. Chica − *Department of Chemistry, Columbia University, New York, New York 10027, United States*

David A. Broadway − *Department of Physics, University of Basel, 4056 Basel, Switzerland; School of Science, RMIT University, Melbourne 3001, Australia*

Cory R. Dean − *Department of Applied Physics and Applied Mathematics, Columbia University, New York, New York 10027, United States*

Xavier Roy − *Department of Chemistry, Columbia University, New York, New York 10027, United States;* orcid.org/0000-0002-8850-0725

Patrick Maletinsky − *Department of Physics, University of Basel, 4056 Basel, Switzerland;* orcid.org/0000-0003-1699-388X

Complete contact information is available at: https://pubs.acs.org/10.1021/acs.nanolett.4c03919

Author Contributions

▽Authors K. Bagani and A. Vervelaki contributed equally to this work.

Notes

The authors declare no competing financial interest.

■ ACKNOWLEDGMENTS

We thank Sascha Martin and his team in the machine shop of the Department of Physics at the University of Basel for their role in building the scanning probe microscope. We also thank Monica Schoenenberger from the Nano Imaging Lab of the Swiss Nanoscience Institute for help with AFM. Calculations were performed at sciCORE (http://scicore.unibas.ch/) scientific computing center at the University of Basel. We acknowledge support of the European Commission under H2020 FET Open grant "FIBsuperProbes" (Grant No. 892427) and ERC Consolidator Grant QS2DM, the SNF under Grant No. 207933 and 188521, and the Canton Aargau. Synthetic work at Columbia was supported by the National Science Foundation (NSF) through the Columbia Materials Science and Engineering Research Center on Precision-Assembled Quantum Materials (No. DMR-2011738). A.D. acknowledges support from the Simons Foundation Society of Fellows program (Grant No. 855186).

REFERENCES

(1) Li, D.; Li, S.; Zhong, C.; He, J. Tuning magnetism at the two-dimensional limit: a theoretical perspective. *Nanoscale* **2021**, *13*, 19812−19827.

(2) Verzhbitskiy, I. A.; et al. Controlling the magnetic anisotropy in $Cr_2Ge_2Te_6$ by electrostatic gating. *Nat. Electron.* **2020**, *3*, 460−465.

(3) Zhuo, W.; Lei, B.; Wu, S.; Yu, F.; Zhu, C.; Cui, J.; Sun, Z.; Ma, D.; Shi, M.; Wang, H.; et al. Manipulating Ferromagnetism in Few-Layered $Cr_2Ge_2Te_6$. *Adv. Mater.* **2021**, *33*, 2008586.

(4) Siskins, M.; Lee, M.; Manas-Valero, S.; Coronado, E.; Blanter, Y. M.; van der Zant, H. S. J.; Steeneken, P. G.; et al. Magnetic and electronic phase transitions probed by nanomechanical resonators. *Nat. Commun.* **2020**, *11*, 2698.

(5) Wang, Y.; Wang, C.; Liang, S.-J.; Ma, Z.; Xu, K.; Liu, X.; Zhang, L.; Admasu, A. S.; Cheong, S.-W.; Wang, L.; et al. Strain-Sensitive Magnetization Reversal of a van der Waals Magnet. *Adv. Mater.* **2020**, *32*, 2004533.

(6) Göser, O.; Paul, W.; Kahle, H. Magnetic properties of CrSBr. *J. Magn. Magn. Mater.* **1990**, *92*, 129−136.

(7) Telford, E. J.; Dismukes, A. H.; Lee, K.; Cheng, M.; Wieteska, A.; Bartholomew, A. K.; Chen, Y.-S.; Xu, X.; Pasupathy, A. N.; Zhu, X.; Dean, C. R.; Roy, X.; et al. Layered Antiferromagnetism Induces Large Negative Magnetoresistance in the van der Waals Semiconductor CrSBr. *Adv. Mater.* **2020**, *32*, 2003240.

(8) Telford, E. J.; et al. Coupling between magnetic order and charge transport in a two-dimensional magnetic semiconductor. *Nat. Mater.* **2022**, *21*, 754−760.

(9) Cenker, J.; et al. Reversible strain-induced magnetic phase transition in a van der Waals magnet. *Nat. Nanotechnol.* **2022**, *17*, 256−261.

(10) Cenker, J. et al. Strain-programmable van der Waals magnetic tunnel junctions. *arXiv Preprints* 2023, arXiv:2301.03759 DOI: 10.48550/arxiv.2301.03759 (accessed Feb. 29, 2024).

(11) Telford, E. J.; Chica, D. G.; Ziebel, M. E.; Xie, K.; Manganaro, N. S.; Huang, C.-Y.; Cox, J.; Dismukes, A. H.; Zhu, X.; Walsh, J. P. S.; Cao, T.; Dean, C. R.; Roy, X.; et al. Designing Magnetic Properties in CrSBr through Hydrostatic Pressure and Ligand Substitution. *Adv. Phys. Res.* **2023**, *2*, 2300036.

(12) Tabataba-Vakili, F.; Nguyen, H. P. G.; Rupp, A.; Mosina, K.; Papavasileiou, A.; Watanabe, K.; Taniguchi, T.; Maletinsky, P.; Glazov, M. M.; Sofer, Z.; Baimuratov, A. S.; Hogele, A.; et al. Doping-control of excitons and magnetism in few-layer CrSBr. *Nat. Commun.* **2024**, *15*, 4735.

(13) Shcherbakov, D.; et al. Raman Spectroscopy, Photocatalytic Degradation, and Stabilization of Atomically Thin Chromium Triiodide. *Nano Lett.* **2018**, *18*, 4214−4219.

(14) Wu, Y.; et al. Degradation Effect and Magnetoelectric Transport Properties in $CrBr_3$ Devices. *Materials* **2022**, *15*, 3007.

(15) Mastrippolito, D.; et al. Emerging oxidized and defective phases in low-dimensional $CrCl_3$. *Nanoscale Advances* **2021**, *3*, 4756−4766.

(16) Lee, K.; et al. Magnetic Order and Symmetry in the 2D Semiconductor CrSBr. *Nano Lett.* **2021**, *21*, 3511−3517.

(17) Tschudin, M. A.; Broadway, D. A.; Siegwolf, P.; Schrader, C.; Telford, E. J.; Gross, B.; Cox, J.; Dubois, A. E. E.; Chica, D. G.; Rama-Eiroa, R.; et al. Imaging nanomagnetism and magnetic phase transitions in atomically thin CrSBr. *Nat. Commun.* **2024**, *15*, 6005.

(18) Bo, X.; Li, F.; Xu, X.; Wan, X.; Pu, Y. Calculated magnetic exchange interactions in the van der Waals layered magnet CrSBr. *New J. Phys.* **2023**, *25*, 013026.

(19) Diao, Y.; et al. Strain-regulated magnetic phase transition and perpendicular magnetic anisotropy in CrSBr monolayer. *Physica E: Low-dimensional Systems and Nanostructures* **2023**, *147*, 115590.

(20) Yang, K.; Wang, G.; Liu, L.; Lu, D.; Wu, H. Triaxial magnetic anisotropy in the two-dimensional ferromagnetic semiconductor CrSBr. *Phys. Rev. B* **2021**, *104*, 144416.

(21) Wang, B.; et al. Origin and regulation of triaxial magnetic anisotropy in the ferromagnetic semiconductor CrSBr monolayer. *Nanoscale* **2023**, *15*, 13402−13410.

(22) Kapfer, M.; et al. Programming twist angle and strain profiles in 2D materials. *Science* **2023**, *381*, 677−681.

(23) Wyss, M.; et al. Magnetic, Thermal, and Topographic Imaging with a Nanometer-Scale SQUID-On-Lever Scanning Probe. *Physical Review Applied* **2022**, *17*, 034002.

(24) Wilson, N. P.; et al. Interlayer electronic coupling on demand in a 2D magnetic semiconductor. *Nat. Mater.* **2021**, *20*, 1657−1662.

(25) Yao, F.; Multian, V.; Wang, Z.; Ubrig, N.; Teyssier, J.; Wu, F.; Giannini, E.; Gibertini, M.; Gutierrez-Lezama, I.; Morpurgo, A. F.; et al. Multiple antiferromagnetic phases and magnetic anisotropy in exfoliated $CrBr_3$ multilayers. *Nat. Commun.* **2023**, *14*, 4969.

(26) Klein, J.; Pham, T.; Thomsen, J. D.; Curtis, J. B.; Denneulin, T.; Lorke, M.; Florian, M.; Steinhoff, A.; Wiscons, R. A.; Luxa, J.; Sofer, Z.; Jahnke, F.; Narang, P.; Ross, F. M.; et al. Control of structure and spin texture in the van der Waals layered magnet CrSBr. *Nat. Commun.* **2022**, *13*, 5420.

(27) Rizzo, D. J.; McLeod, A. S.; Carnahan, C.; Telford, E. J.; Dismukes, A. H.; Wiscons, R. A.; Dong, Y.; Nuckolls, C.; Dean, C. R.; Pasupathy, A. N.; et al. Visualizing Atomically Layered Magnetism in CrSBr. *Adv. Mater.* **2022**, *34*, 2201000.

(28) Vansteenkiste, A.; Leliaert, J.; Dvornik, M.; Helsen, M.; Garcia-Sanchez, F.; Van Waeyenberge, B.; et al. The design and verification of MuMax3. *AIP Adv.* **2014**, *4*, 107133.

(29) Exl, L.; Bance, S.; Reichel, F.; Schrefl, T.; Peter Stimming, H.; Mauser, N. J.; et al. LaBonte's method revisited: An effective steepest descent method for micromagnetic energy minimization. *J. Appl. Phys.* **2014**, *115*, 17D118.

(30) Zur, Y.; Noah, A.; Boix-Constant, C.; Manas-Valero, S.; Fridman, N.; Rama-Eiroa, R.; Huber, M. E.; Santos, E. J. G.; Coronado, E.; Anahory, Y.; et al. Magnetic Imaging and Domain Nucleation in CrSBr Down to the 2D Limit. *Adv. Mater.* **2023**, *35*, 2307195.

(31) Qiao, L.; et al. Curvature-induced magnetization in a CrI_3 bilayer: Flexomagnetic effect enhancement in van der waals antiferromagnets. *Phys. Rev. B* **2024**, *109*, 014410.

(32) Yu, J.; Liu, D.; Ding, Z.; Yuan, Y.; Zhou, J.; Pei, F.; Pan, H.; Ma, T.; Jin, F.; Wang, L.; et al. Direct Imaging of Antiferromagnet-Ferromagnet Phase Transition in van der Waals Antiferromagnet CrSBr. *Adv. Funct. Mater.* **2024**, *34*, 2307259.

(33) Boix-Constant, C.; et al. Multistep magnetization switching in orthogonally twisted ferromagnetic monolayers. *Nat. Mater.* **2024**, *23*, 212−218.

https://doi.org/10.1021/acs.nanolett.4c03919
Nano Lett. XXXX, XXX, XXX−XXX